

Grayscale lithography—automated mask generation for complex three-dimensional topography

James Loomis
Dilan Ratnayake
Curtis McKenna
Kevin M. Walsh

Grayscale lithography—automated mask generation for complex three-dimensional topography

James Loomis,^{a,*} Dilan Ratnayake,^b Curtis McKenna,^b and Kevin M. Walsh^{b,*}

^aUniversity of Auckland, Department of Mechanical Engineering, 20 Symonds Street, Auckland 1010, New Zealand

^bUniversity of Louisville, Department of Electrical and Computer Engineering, W.S. Speed Hall 200, Louisville, Kentucky 40292, United States

Abstract. Grayscale lithography is a relatively underutilized technique that enables fabrication of three-dimensional (3-D) microstructures in photosensitive polymers (photoresists). By spatially modulating ultraviolet (UV) dosage during the writing process, one can vary the depth at which photoresist is developed. This means complex structures and bioinspired designs can readily be produced that would otherwise be cost prohibitive or too time intensive to fabricate. The main barrier to widespread grayscale implementation, however, stems from the laborious generation of mask files required to create complex surface topography. We present a process and associated software utility for automatically generating grayscale mask files from 3-D models created within industry-standard computer-aided design (CAD) suites. By shifting the microelectromechanical systems (MEMS) design onus to commonly used CAD programs ideal for complex surfacing, engineering professionals already familiar with traditional 3-D CAD software can readily utilize their pre-existing skills to make valuable contributions to the MEMS community. Our conversion process is demonstrated by prototyping several samples on a laser pattern generator—capital equipment already in use in many foundries. Finally, an empirical calibration technique is shown that compensates for nonlinear relationships between UV exposure intensity and photoresist development depth as well as a thermal reflow technique to help smooth microstructure surfaces. © 2016 Society of Photo-Optical Instrumentation Engineers (SPIE) [DOI: 10.1117/1.JMM.15.1.013511]

Keywords: photolithography; grayscale; three-dimensional microelectromechanical systems; laser pattern generator; automated conversion; thermal reflow.

Paper 15191 received Dec. 8, 2015; accepted for publication Mar. 3, 2016; published online Mar. 23, 2016.

1 Introduction

The market value for silicon-based microelectromechanical systems (MEMS) devices is forecasted to grow from \$11 billion in 2014 to \$20 billion in 2020.¹ Even so, the MEMS industry remains highly fragmented, with few applications having markets greater than \$200 million.² While impressive numbers, it is possible that this market could actually be much larger. As noted in a 2012 Massachusetts Institute of Technology (MIT) news article, due to the high costs associated with commercializing innovative designs (specifically capital equipment costs), many experimental MEMS devices do not have market potentials large enough to justify building new manufacturing facilities.³ Therefore, development of enhanced cost reduction tools and techniques are essential to bring next generation MEMS technologies to fruition. In this paper, we demonstrate a process and associated software to improve the capabilities of existing, operational equipment. This process entails an automated method to create grayscale lithography masks files for complex three-dimensional (3-D) microstructures necessary for the next generation of MEMS devices. The process is demonstrated here by direct writing on a laser pattern generator (LPG) for a number of structures. This method is suitable for prototyping MEMS devices but impractical for volume production due to long write times. To transition from prototyping to commercial applications, however, several implementations of this process may be possible. For example, optical grayscale photomasks can

be fabricated on high-energy-beam-sensitive glass through electron-beam (e-beam) lithography. Alternatively, this conversion process can be used to create complex 3-D molds (either directly or indirectly), which in turn can be used for volume production manufacturing processes, such as injection molding, microstamping, nanoimprinting, and polydimethylsiloxane processing.

MEMS processes and designs have traditionally evolved from IC-based fabrication techniques, which require only planar [two-dimensional (2-D)] structures be fabricated as there are essentially no mechanical operations taking place in the out-of-plane direction.⁴ MEMS devices traditionally utilize nominally vertical sidewalls (dry anisotropic etching),⁵ undercut sidewalls (wet isotropic etching),⁶ or sidewalls that have limited 54.74-deg angles due to the crystallographic orientation of the substrate (wet anisotropic etching).⁷ However, improved methods of fabricating 3-D structures with arbitrary but controllable depth profiles (normal to the substrate surface) will enable new devices to be proposed with enhanced optical, mechanical, and electrical properties at lower costs. Several such technologies and processes have been introduced to fabricate more complex 3-D MEMS structures. These processes encompass a combination of direct-writing,^{8–11} photolithography,^{12,13} etching,^{14–16} micromachining,^{17–19} and wafer bonding.^{20,21} Of course, more complex 3-D structures are possible with multiple lithography steps; however, this dramatically increases fabrication time and device cost.²²

*Address all correspondence to: James Loomis, E-mail: j.loomis@auckland.ac.nz; Kevin M. Walsh, E-mail: kevin.walsh@louisville.edu

Even with the numerous technologies previously listed, the design of arbitrary 3-D microstructures is highly restricted using planar fabrication processes. However, grayscale lithography, a technique used to fabricate complex structures and topography from a single lithographic exposure, is an attractive option. While traditional photolithography is characterized by the binary exposure of the photoresist, grayscale lithography can spatially modulate UV exposure to accurately control development depth. As such, grayscale presents an intriguing method of generating complex arbitrary surface geometry in photosensitive polymers, such as photoresist. Additionally, due to the single exposure process, grayscale photolithography is more efficient and does not suffer from potential alignment errors associated with multiple masks.²³ Furthermore, complex geometries can be obtained from a single lithographic exposure employing microfabrication equipment already in use in industrial foundries. Numerous research works covering a variety of grayscale methods have been published. Among these works, Kirchner et al.²⁴ utilized a combination of e-beam grayscale lithography combined with a selective thermal reflow to obtain smooth bioinspired 3-D structures. Other grayscale lithography techniques include grayscale photolithography (UV lithography), such as grayscale e-beam lithography²⁵ and grayscale x-ray lithography.²⁶ In addition, methods have also been demonstrated for transferring arbitrary surface topography from temporary photoresists to a permanent medium (i.e., the substrate) through anisotropic etching, such as deep reactive-ion etching (DRIE) or reactive-ion etching (RIE) tools.^{27–29} Previous work at the University of Louisville included maskless grayscale lithography for MEMS applications using a polyimide (HD-8820).³⁰ Most of these studies, however, were limited geometries and specific applications, such as microfluidics,³¹ biomedical,³² and microtools.³³

An interesting opinion piece by Kirchner and Schiff³⁴ questions why binary (traditional) photolithography for commercial manufacturing is a well-established technology, yet 3-D micro-/nanopatterning is not. Furthermore, they argue that high resolution, high fidelity molding will enable 3-D lithography designs to transition from niche applications to commercial production.³⁴ One contributing factor for this lack of widespread implementation may be the lack of standardized methods for creating complex grayscale mask files. To the best of the authors' knowledge, mask files used in LPGs must be created manually, a time-consuming process that places severe limitations on design complexity and overall usefulness. For simple 3-D shapes, such as a ramp or dome, mask files are relatively straightforward. Consider, for example, the Heidelberg 66FS, a maskless lithography LPG that features 128 levels of UV intensity (z resolution). In the best case scenarios, to discretize simple structure geometries, the number of elements needed to define the shapes can generally be reduced to one per layer (or about 128 elements total). While this method may be somewhat tedious, it is certainly feasible to calculate dimensions for this number of elements manually. As desired microstructures evolve beyond such simplistic designs, however, manual creation of mask files becomes unrealistic. If the LPG is set up with a 250 nm \times 250 nm address grid (xy resolution or pixel size), even a 100 μm \times 100 μm structure can require up to 1.6×10^5 rectangular elements, with

each element requiring five pieces of information (coordinates of the four vertices and layer number). Furthermore, if multiple design iterations are desired (such as an array of ramps, each with a variable slope), an automatic mask generation technique is crucial and necessitates development of an easily implemented automated process for producing mask files of complex 3-D topography.

In this paper, we present the development of an automated process and corresponding software utility for generating these complex grayscale mask files. This grayscale conversion (GSC) application-agnostic process encompasses four key innovations: (1) enable MEMS design using commercially available computer-aided design (CAD) software; (2) automatic mask conversion to allow for complex microstructure topographies; (3) map and compensate for nonlinear photoresist effects; and (4) compatible with existing, in-place semiconductor processing equipment—thus successfully demonstrating a commercially attractive method for creating complex topography profiles in photoresist in a single lithographic exposure.

2 Solid Model to Mask File Conversion Process

Figure 1 presents a simplified overview of the GSC process presented in this manuscript with each step described in detail in the following sections. Process development and fabrication was performed at the University of Louisville Micro/Nano Technology Center (MNTC), a 10,000 ft² class 100/1000 cleanroom facility and part of the new National Nanotechnology Coordinated Infrastructure (NNCI). To demonstrate applicability toward eventual commercial deployment and as an aid for explaining the process in this paper, a software interface was written to automate and simplify the GSC process for end users [Fig. 1(a) shows a screenshot].

To start, a desired 3-D structure is designed using any number of commercially available CAD software packages. For simplification and ease of use, the structure design may use any size scale and unit system (given that consistency is maintained throughout) as model scaling occurs later in the conversion utility. Figure 1(b) shows an example of a desired microstructure (blue dome) sitting on a gray dummy wafer substrate (model created in SolidWorks, note that the colors are arbitrary). While the specific models shown were chosen for presentation clarity, note that any complex surface topography is possible subject to the restrictions detailed in Sec. 2.2. Once modeling of the desired structure is completed in the CAD software, it is exported to a stereolithography (STL) file. An STL file format was chosen as this format is widely utilized throughout industrial and rapid prototyping communities for sharing 3-D model geometry.³⁵ More specifically, the STL file stores surface morphology of an object by means of a triangular mesh, with each triangle defined by the three boundary points plus an outward normal.³⁶ The GSC software utility was written to accept STL files, and during the conversion is responsible for determining orientation of the substrate/wafer section and then slicing the model into a discrete number of layers [Fig. 1(c)]. The total number of possible layers (n) is defined by the UV modulation capabilities of the LPG (typically 128) and represents the grayscale “resolution” in the vertical (z) direction. The GSC software sets the first layer (n_0 , 0% exposure intensity) coincident with

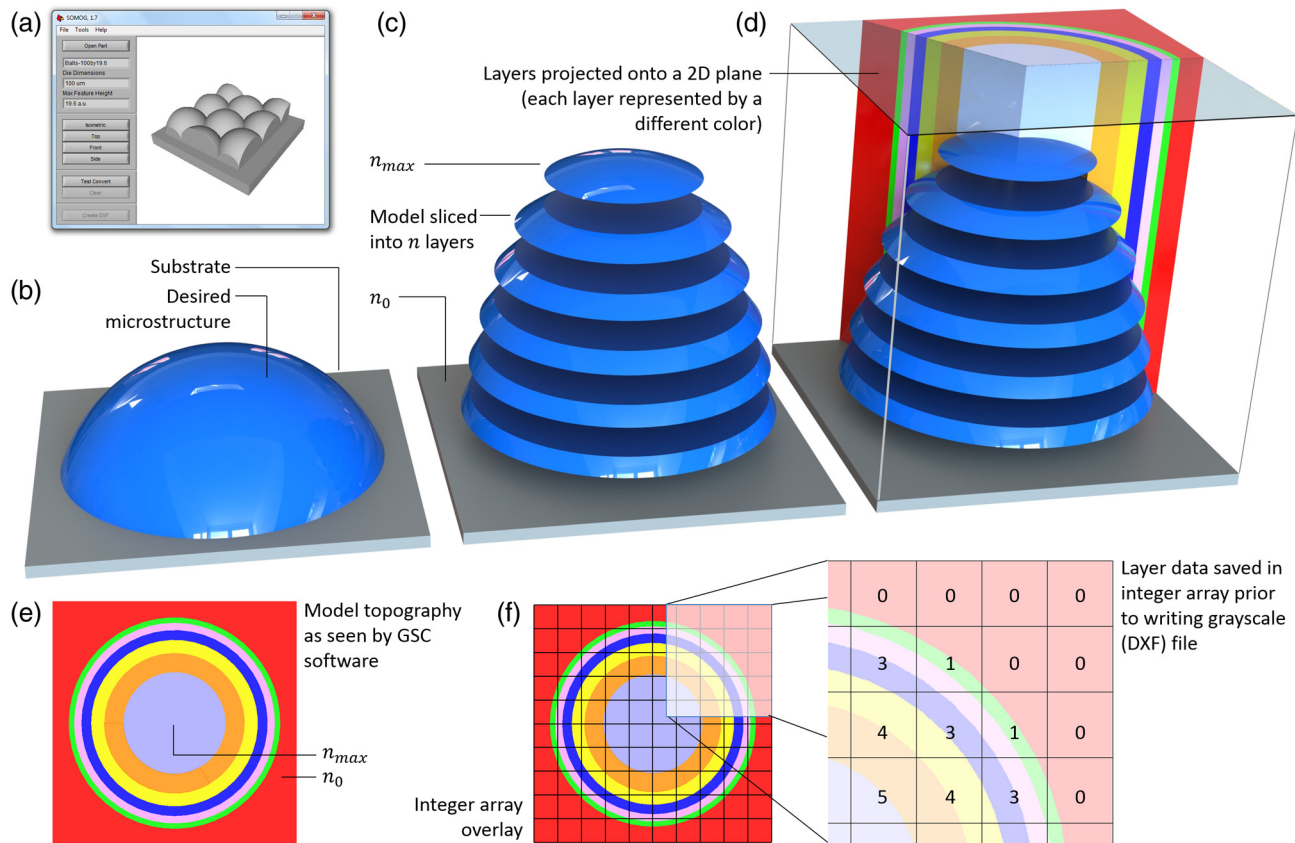


Fig. 1 GSC process overview: (a) screenshot of GSC software utility with sample CAD model loaded, (b) sample 3-D structure created in CAD program, (c) sample structure is sliced into n layers (n governed by LPG capabilities), (d) 2-D plane is created above the structure, and the layer information is projected, (e) CAD model topography as seen by the GSC software, and (f) projection plane overlaid with $N \times M$ integer array, and detail showing array populated with layer numbers.

the substrate surface and the maximum layer (i.e., n_{max} or n_{127} , 100% exposure intensity) coincident to the highest point of the model and parallel to the substrate. Individual layers are then scaled between n_0 and n_{max} , and feature non-uniform thicknesses that are determined based on a combination of user-set conversion variables and calibration results. Due to a change in the complex index of refraction in photoresist to UV illumination, which creates nonlinear exposure/development profiles,³⁷ actual part conversion first requires an initial calibration step. This additional step maps and compensates for nonlinearities when calculating layer thicknesses (detailed in Sec. 2.1). Once model segmentation is complete, a 2-D plane identical in size to the substrate footprint is placed above the model; and each layer is projected onto the plane, creating a topographic map of the microstructure [Figs. 1(d) and 1(e)]. An $N \times M$ integer array is overlaid on the projection plane [Fig. 1(f)], with the number of elements in the N and M directions LPG resolution dependent. In this manner, each element can be thought of as a “pixel,” and the portion of the topographic projection image contained within each element converted to its integer equivalent. Note that resolutions are equipment-based and not a fundamental limitation of the conversion technique presented. Finally, the 2-D array information is converted into a drawing exchange format (DXF) file in accordance with Autodesk standards (a file format compatible with many commercial LPGs).³⁸

Regardless of 3-D microstructure geometry, the GSC process follows four general steps: (1) determine the processing parameters and run a standardized calibration structure; (2) create a CAD model of the desired microstructure; (3) import the calibration map into the GSC software and perform model conversion; and (4) write the grayscale DXF file on the LPG.

2.1 Calibration

A calibration step is required to map the nonlinear (photoresist/processing dependent) correlation between UV exposure intensity and photoresist development depth. This information is crucial for correctly adjusting layer segmentation in the GSC process, a necessary step as most photoresists are not chemically engineered for grayscale lithography. The nonlinear relationship is assumed to vary depending on a given set of process variables—i.e., photoresist type, spin speed/time, soft bake time, LPG settings, and so on. Ideally, a multivariable analysis (using principal component analysis or similar technique) would provide a generalized model to identify the effect each physical process variable has on development depth. For the work presented in this manuscript, however, a simplified univariable mode of photoresist development depth was chosen. This simplified model was selected for clarity in presenting the conversion method and resulted in the calibration procedure described henceforth. As such, when using this

method, the authors recommend a new calibration whenever there is a change in any aspect of the photoresist processing. If the only aspect changing is the CAD model, however, a new calibration is “not” required. Before evaluating nonlinearities in the photoresist, equipment and processing variables require evaluation. The thickness of the photoresist and maximum UV exposure intensity need to be balanced such that applied LPG beam intensity has the ability to expose both partially and fully through the photoresist. This is an equipment-based step involving LPG setup and photoresist deposition parameters. For example, if at the maximum UV exposure intensity development occurs only through a fraction of the total available photoresist thickness, problems in postprocessing may occur. If the structure is being used for mold transfer, however, this may be acceptable if total development depth is adequate. Likewise, if the entirety of the photoresist is developed before the maximum LPG exposure levels, then multiple layers will register as fully exposed in the fabricated device and a portion of the topography features will be lost.

The mapping process entails writing a standardized grayscale file (in this case, a ramp structure) on the LPG using the same photoresist, processing parameters (spin speed/time, soft bake, and so on), and optical setup as the planned device. Any calibration structure geometry can be used provided that it is sufficient to establish a relationship between desired and experimental development depth. A ramp-type structure, however, provides a natural means to obtain such a relationship. After fabricating the calibration structure, its development depth profile is measured to obtain the experimental exposure depth (d_i) versus exposure intensity relationship as n_i ranges from n_0 to n_{max} . The key in the calibration step is to first assume a “linear” (ideal) exposure/development depth profile. A calibration relationship is established by comparing differences in development depth of the i 'th layer between the experimental data and linear (or “ideal”) profiles. Profile data from the fabricated calibration ramp structure should exhibit easily identifiable and distinct “steps” corresponding to each change in exposure intensity [Fig. 2(a)]. In reality, the authors experienced mixed success

in this regard (mainly depending on type of photoresist used), and therefore, a generalized curve fitting process is later described that applies to all cases.

Horizontal ramp length (L) is already known from the design of the calibration structure, and maximum photoresist development depth (D) can be obtained from a profilometer scan. Using these values, an ideal linear fit is determined [Eq. (1) and Fig. 2(a)] that provides the development depth profile that would result given the ideal initial assumptions stated previously—a linear photoresist exposure/development relationship, where x equals distance from the start of the ramp [indicated by “structure start” on Fig. 2(a)]. Using MATLAB, an n 'th order polynomial (in this case $n = 5$) was fit to a single experimental profilometer scan (2.7×10^4 data points, $R^2 = 0.975$) and shown plotted against the ideal case [Eq. (2) and Fig. 2(b)]. The horizontal ramp length is $10 \mu\text{m}$ and development depth is $4 \mu\text{m}$ (AZ4620 photoresist). Note that while the two curves agree relatively closely through the first half of the ramp structure, discrepancies become especially evident at higher UV intensities. Equation (3) gives the nonlinearity error (ϵ) in the experimental structure. While the calibration goal is to collapse $f(x)_{exp}$ onto $f(x)_{ideal}$ such that the experimental profile emulates the ideal profile as close as possible, the challenge is that the LPG has a limited number of discrete UV exposure intensity settings (i.e., 128), where each results in a “layer” with a fixed development depth:

$$f(x)_{ideal} = -\left(\frac{D}{L}\right)x, \quad (1)$$

$$f(x)_{exp} = ax^5 + bx^4 + \dots + f, \quad (2)$$

$$\epsilon = [f(x)_{exp} - f(x)_{ideal}] / f(x)_{ideal}. \quad (3)$$

Therefore, the only means to modify $f(x)_{exp}$ is through tuning layer thicknesses to collapse it onto the ideal, linear curve. The first step is determining actual experimental development depth (d_i) of each layer in the fabricated

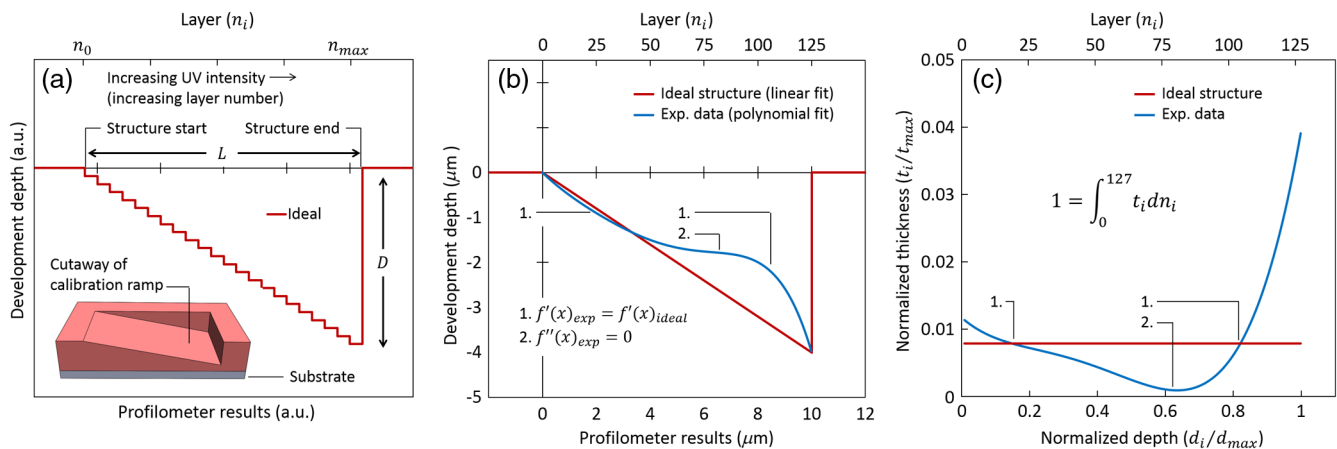


Fig. 2 Calibration detail for AZ4620 photoresist. (a) Profile of ideal (stepped) calibration structure. Note that for clarity, the number of layers (n) has been reduced and layer thicknesses (t_i) exaggerated. (b) Initial (uncalibrated) profilometer of actual ramp structure showing discrepancy between ideal and experimental development at higher UV exposure intensity. (c) Calibration plot showing normalized layer thicknesses.

ramp structure. Equation (4) provides discrete values of d_i by evaluating the experimental fit function at x values corresponding to each layer of the fabricated test structure (x_i). Stated another way, d_i is the “actual experimental” development depth of the i ’th layer (n_i) for the real-world system. Furthermore, d_i is a fixed value, and there is no way to alter it for a given setup. If a different depth profile is desired, some physical aspect of the grayscale writing process must be changed. Therefore, the only method to collapse the experimental data onto the ideal data is to adjust layers’ thicknesses during the conversion process. Instead of linear segmentation, which was assumed for the ideal structure, CAD model features should be “pushed” to a layer based on the d_i array. Since the GSC process scales layers based on the maximum height of the microstructure (where n_0 represents the wafer surface and n_{\max} the model’s peak), normalized layer thicknesses (t_i) are required [Eq. (5)]. The plot in Fig. 2(c) shows normalized “ideal” and “experimental” layer thicknesses versus layer number and normalized depth (note that the integral of each curve equals one).

$$d_i = f_{\text{exp}}\left(\frac{n_i L}{n_{\max}}\right) \quad \text{for } i = 0 \text{ to } n_{\max}, \quad (4)$$

$$t_i = \left| \frac{1}{D} (d_i - d_{i-1}) \right| \quad \text{for } i = 1 \text{ to } n_{\max}. \quad (5)$$

There are several important consequences of the nonlinear exposure relationship demonstrated by the experimental structure. First and most obvious is the inconsistency of depth resolution of different layers. For example, this inconsistency is highlighted when comparing experimental and ideal profiles. While first-order derivatives for the ideal and experimental fit functions are “equal” [point 1 in Figs. 2(b) and 2(c)], experimental layer thickness is approximately “equal” to the ideal case. However, when the first-order derivative for experimental is “greater than” the ideal case, this relationship signifies that real-world resolution in this region is “coarser,” or worse than the ideal case. Likewise, when the first-order derivative for experimental is “less than” ideal, real-world resolution in this region is “finer,” or better than the ideal case. Taking the second-order derivative of the experimental fit function, the inflection point provides a local minimum that shows the region of highest z resolution (Table 1 provides a summary). For example, in the ideal case, each layer has an identical

Table 1 Depth resolution relationships between experimental and ideal exposures.

$f'(x)_{\text{exp}} = f'(x)_{\text{ideal}}$	Experimental z resolution is “equal to” the ideal case
$ f'(x)_{\text{exp}} > f'(x)_{\text{ideal}} $	Experimental z resolution is “coarser than” the ideal case
$ f'(x)_{\text{exp}} < f'(x)_{\text{ideal}} $	Experimental z resolution is “finer than” the ideal case
$f''(x)_{\text{exp}} = 0$	Region of highest z resolution

thickness [horizontal line in Fig. 2(c)], meaning that the z resolution of the structure is identical throughout. If this was reality, writing layer 64 out of 128 (50% UV intensity) would result in photoresist developing to half the total depth. Unfortunately, the experimental data confirm that this is not the case. Rather, in the initial 20 layers, resolution is much coarser as the thickness of the experimental layers exceeds that of the ideal. In the middle region (between layers 21 and 105), however, experimental layer thicknesses are much finer than the ideal, resulting in better resolution in this region. Finally, from layer 106 onward, each experimental layer becomes quite thick, indicating poor resolution and extremely coarse features. Overall, this means that when designing structures, engineers should be cognizant of this depth profile and if possible, try to concentrate key design features in regions with the best z resolution. These calibration results should be valid for any grayscale lithography fabricated with identical processing variables as the calibration structure. When a parameter changes (for example, spin speed), however, it is prudent to perform a new calibration and re-verify.

2.2 Microstructure Design

While the GSC software presented here was written such that 3-D models (parts or assemblies) can be generated in any CAD software capable of exporting to the STL format, there are several design considerations necessary for proper process implementation. Starting off, a neutral plan (or simulated “wafer” substrate) is required [Fig. 3(a)] as the GSC software relies on this plane to define the conversion bounds. Since a 2-D integer array is utilized for writing the final DXF file, this substrate must be a square or rectangular shape with a footprint equal to or exceeding that of the desired microstructure. One necessary consideration needed if a substrate is added after the initial part design, such as in an assembly, is that the top plane of the substrate forms a lower boundary for the conversion process. Thus, any portion of the model coincident to or below top plane of the substrate (or for example, extending out the bottom) will not be “seen” by the GSC software. As such, thickness of the substrate modeled in the negative z direction is irrelevant.

Because of how the conversion software was written (and in order to mimic real-world LPG writing restrictions), the output grayscale file represents a topographical map of the model with relief contours resulting from layer segmentation. The repercussion with respect to part design is that only features visible from a “top view” of the model/assembly will be written to the grayscale file, meaning that features, such as undercuts or enclosed voids/cavities, will not be converted and all information regarding these elements lost. For example, Fig. 3(a) shows a sample part that features a void underneath a bridge-type structure. When viewing this part from a topographical view [Fig. 3(b)], this open-space feature is no longer visible and therefore during conversion will be “erased.” To illustrate this point, the structures shown in Figs. 3(a) and 3(c) will produce identical grayscale mask files using this GSC process.

Finally, since the STL file format strips all superfluous information about the model and only saves surface geometry, the units or scale used is irrelevant as long as consistency is maintained within the model in the xy direction (scaling is set during the conversion process). For example,

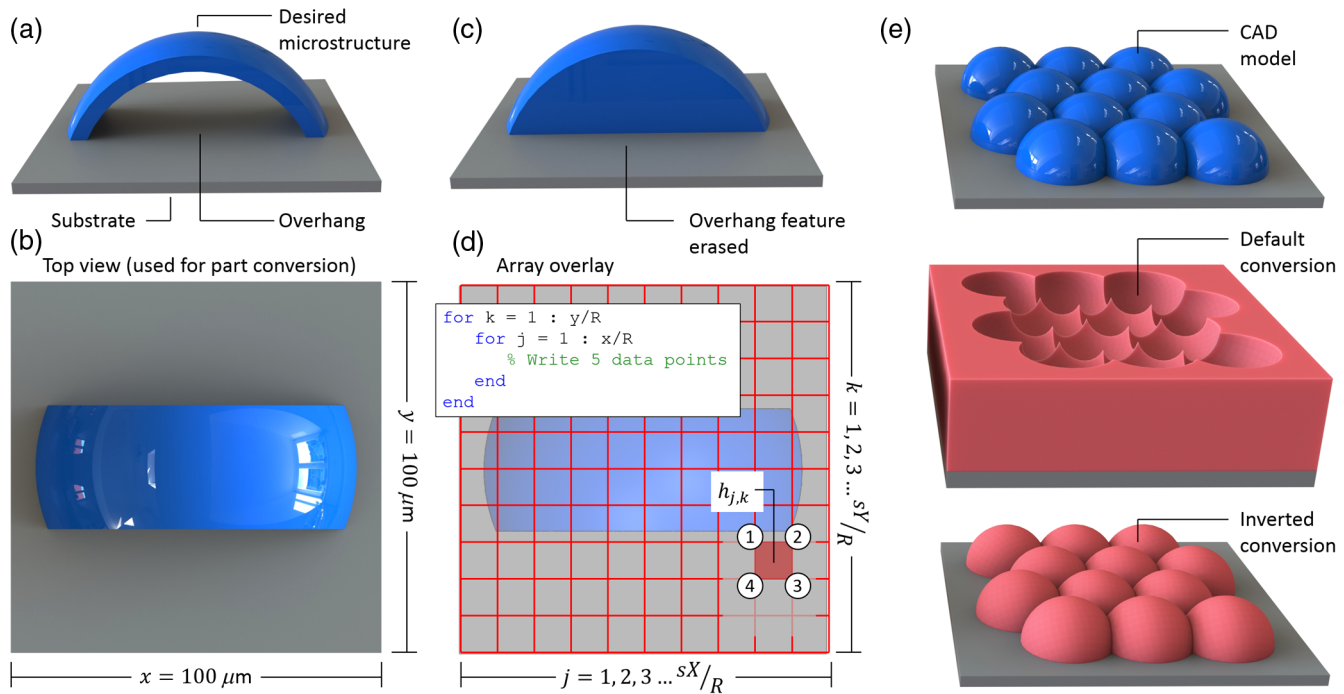


Fig. 3 Design considerations and conversion detail. (a) Initial sample structure designed with an enclosed/overhanging feature. (b) Top view of CAD model, simulating what is observed by the GSC software. (c) Modified model showing the more realistic version of the actual structure that will be fabricated. (d) Detail of integer array that will be created and list of the five parameters written to the mask file for each element. (e) Hemisphere array CAD sample (top), and models of default (middle) and inverted (bottom) photoresist conversion mask options in the GSC software.

when designing a part in CAD, a square substrate of 100 in. per side will result in a model identical to one designed with 100 m per side and will be read by the GSC software utility as 100 “units” per side; final dimensions for conversion (in μm) are set by the user. Furthermore, since the GSC process does not make any distinction regarding depth of the photoresist layer, scaling in the z direction is somewhat arbitrary and does not necessarily need to correlate to the scale chosen for the xy dimensions. Rather, the conversion process scales the z direction such that the substrate surface is coincident with the first layer (n_0), and the maximum layer (n_{max}) set to the highest point of the structure. Individual layer thicknesses are calculated based on the previously described calibration process. Therefore, it is merely the relative height of features with respect to one another that matters, and features in the z direction can be exaggerated without consequence if this exaggeration aids in the design stage.

2.3 Grayscale Conversion Software Utility

While the actual conversion process is fairly straightforward, the need to repeat an identical series of steps up to several million times necessitated writing a software utility to streamline the process. This GSC utility enables fast, automated generation of DXF files (suitable for a variety of LPGs) and is used in the follow-on experimental fabrications. Stated simply, the GSC software stores surface topology data from the 3-D CAD model in a 2-D integer array containing layer assignments. This integer array is then written to a mask file in a format suitable to a particular grayscale lithography device (typically DXF). The machine uses the mask data to essentially control relative UV laser

exposure levels or values for the grayscale lithography device at a plurality of locations along the surface of a die, wafer, or other substrate.

Once layer thicknesses have been determined through calibration, actual model conversion to grayscale begins. Starting with the topographic view of Fig. 3(b), the GSC software first creates a 2-D plane above the CAD model with a footprint equal to the bounds of the wafer section. Next, an $N \times M$ integer array is placed coincident to the plane with the number of elements in the array governed by $N = sX/R$ and $M = sY/R$, where X and Y are the unitless dimensions of the wafer footprint (from the STL file), R is the LPG address grid resolution, and s is a user-provided scaling factor (such that sX and sY provide the desired structure footprint in microns). Although this process enables scaling to a particular microstructure size regardless of initial CAD model setup, consideration must be taken when exporting the STL file to ensure that the resolution adequately captures the features. By tying dimensions of the integer array to the LPG address grid size, each array cell can be thought of as a “pixel” with a height and width equal to the resolution value [Fig. 3(d)]. This relationship greatly simplifies calculation of element positions when writing the DXF file. For the example shown assuming a 250-nm LPG address grid and a square wafer substrate of 100 μm /side, a 400×400 integer array will be created with 1.6×10^5 elements. Square elements were chosen as they are most suitable toward writing various grayscale files types (DXF, bitmaps, and so on). Next, to convert the CAD model into a representative set of layer numbers, the 2-D array is indexed, first by column then by row, and height of the feature present within each element ($h_{j,k}$) measured. Equation (6) scales the

elemental height as a function of the maximum feature height present in the CAD model (h) and assigns a layer number based on the calibration development depth profile. This process creates a default negative (inverse) of the original CAD model, with top of the photoresist equivalent to the simulated substrate [Fig. 3(e), assuming positive photoresist]. The option also exists to invert the layers in order to fabricate a microstructure similar to the original CAD design:

$$n_i = \begin{cases} 0 & \text{if } h_{j,k} = 0 \\ i & \text{if } |d_{i-1}| < \frac{h_{j,k}}{h} < |d_i| \end{cases} \quad \text{for } i = 1 \text{ to } n_{\max}. \quad (6)$$

Upon completion of populating the integer array with layer numbers, a grayscale mask file is created, starting with the appropriate structure (header, classes, tables, blocks, entities, objects, and so on); followed by writing element data to the file by indexing the integer array first by column, then by row; and finally closing with appropriate end-of-file markers. To scan the integer array, two nested “for loops” acquire five pieces of information for each array element [Fig. 3(c)]—these include physical locations of the four vertices plus the layer number (Table 2).

While a grayscale mask file for a single dome is relatively straightforward, even with relatively simple surface topography [such as a hemisphere array of connected domes, Fig. 4(a)] manual creation is prohibitively complex. Figures 4(b) and 4(c) show the intricacy associated with even a small $100 \mu\text{m} \times 100 \mu\text{m}$ structure. Note that since

the number of integer array elements scales exponentially with the substrate size being converted, several considerations should be taken into account. First, the current iteration of the GSC software utility scales the array in a single operation. Excessively large array sizes may cause memory-dependent issues in the computer running the software. While not implemented in the software utility presented here, one such solution is to piecewise convert the structure—loading sections of the array, then clearing the buffer before proceeding to the next portion of the model. Second, regarding file compression, adjacent array elements on the same layer can be merged prior to writing the DXF file (this merging method was incorporated into the software utility), which can greatly reduce total number of elements written and hence final file size. For example, 20 adjacent array elements on the same layer can be reduced from 100 data points to just 5 required to define the combined larger element.

2.4 Fabrication

This experiment was performed using a Heidelberg 66FS LPG. Traditionally, Heidelberg LPGs are suited only for binary exposures; but this machine has added functionality that allows for modulating laser intensity during the writing process. This feature enables use of the 66FS toward grayscale lithography to create more complex 3-D structures. The LPG employs either a diode laser ($\sim 405 \text{ nm}$) or a HeCd laser (442 nm), and laser output power is between 20 and 180 mW, depending on specific design. This LPG system features a software package to import a variety of source files, such as Gerber, DXF, crystallographic information file, GDSII, Hewlett-Packard Graphics Language or structure format into the Software License File (LIC) format the machine needs as input.³⁹ During exposure, this LIC format data is converted in real time into the final pixel data. Theoretically, the original design data could be converted directly to the final pixel set, but the advantage of the LIC format is that its file size is much smaller due to a highly optimized compression, leading to a much faster data transfer from the workstation to the system.³⁹ Ultimately, resolution of the patterned grayscale design depends on the writing head used in the LPG. The University of Louisville MNTC currently has three different write heads in their inventory, where the heads are specified by the focal length (distance

Table 2 Integer array element information.

Data point	Description	x coordinate	y coordinate
1	Vertex 1	$R(j-1)$	$R(k-1)$
2	Vertex 2	Rj	$R(k-1)$
3	Vertex 3	Rj	Rk
4	Vertex 4	$R(j-1)$	Rk
5		Layer n_i	

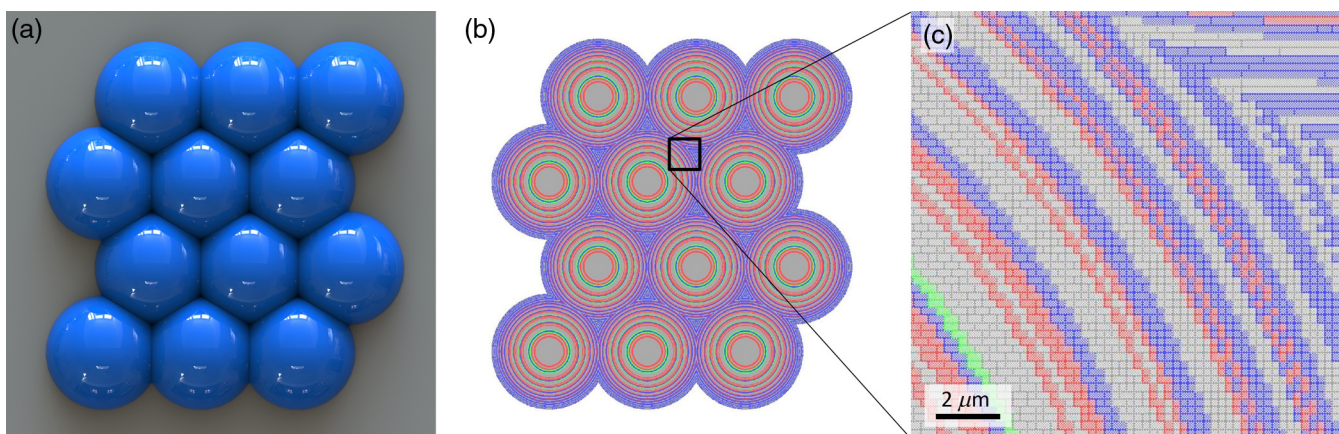


Fig. 4 Grayscale mask complexity detail. (a) Top view of hemisphere array CAD model. (b) Resulting grayscale mask after processing. (c) Detail of mask (250-nm address grid on a $100 \mu\text{m} \times 100 \mu\text{m}$ die).

Table 3 Heidelberg 66FS specifications.

	2	4	20
Focal length of the head (mm)	2	4	20
Minimum feature size (μm)	0.6	1	5
Address grid (nm)	50	100	250
Write speed (cm^2/h)	0.7	3.0	73.2

from the head when the beam is in ideal focus, shorter distances indicate a tighter beam). Table 3 presents minimum feature sizes. The 20-mm head writes faster than other heads, whereas the 2-mm head writes slower than other heads. The address grid defines the smallest feature that the LPG will even attempt to write, anything smaller is completely ignored when compiling the design.

For the examples presented in this work, two photoresists were used—Shipley 1827 and AZ4620 (both positive photoresists). Photoresist layers were spun onto cleaned 4" silicon wafers in accordance with manufacturers' specifications, resulting in layer thicknesses of $\sim 2.7 \mu\text{m}$ and 4 to 20 μm , respectively. A Veeco Dektak 8M Profilometer was used to scan the profile of the structures, and a Zygo Optical Interferometer was used to generate 3-D images of the fabricated structures. The GSC software utility was written and deployed as an executable using a combination of MATLAB and National Instruments LabVIEW Professional Development System.

3 Results and Discussion

Figures 5(a1) and 5(a2) show a series of profilometer scans obtained from 300- μm diameter dome structures (AZ4620 photoresist). As clearly visible in the uncalibrated structure [Fig. 5(a1)], depth resolution is not very consistent. This structure was fabricated using identical thickness layers, meaning no compensation for nonlinear exposure effects. Discontinuities in the surface profile may be a result of stitching errors from neighboring passes of the laser interfering with each other and either overexposing or underexposing portions of the photoresist during the writing process (and not due to nonlinearities of the photoresist). After calibration [Fig. 5(a2)], however, a vastly improved profile is obtained. This figure also shows a profilometer scan after chemical reflow processing. Due to ongoing parallel research by the authors at the MNTC into buckled MEMS devices, in some cases, it is necessary to have extremely smooth photoresist surfaces for follow-on material deposition. Therefore, an additional processing technique, thermal reflow, was used. This process entails controlled heating of the photoresist layer. Viscosity of the photoresist decreases rapidly at temperatures above the glass transition temperature, causing small amounts of photoresist to reflow to minimize surface tension.⁴⁰ This reflow process is a required technique in micro optics and often used to transfer lens shaped structures into the substrate using dry etch. If the substrate is glass, the transferred features can act as lenses in micro-optics applications.^{41,42} Increasing the level of microstructure complexity, Figs. 5(b1) and 5(c1) show CAD models of a logo and hemisphere array, respectively. Figures 5(b2) and 5(c2)

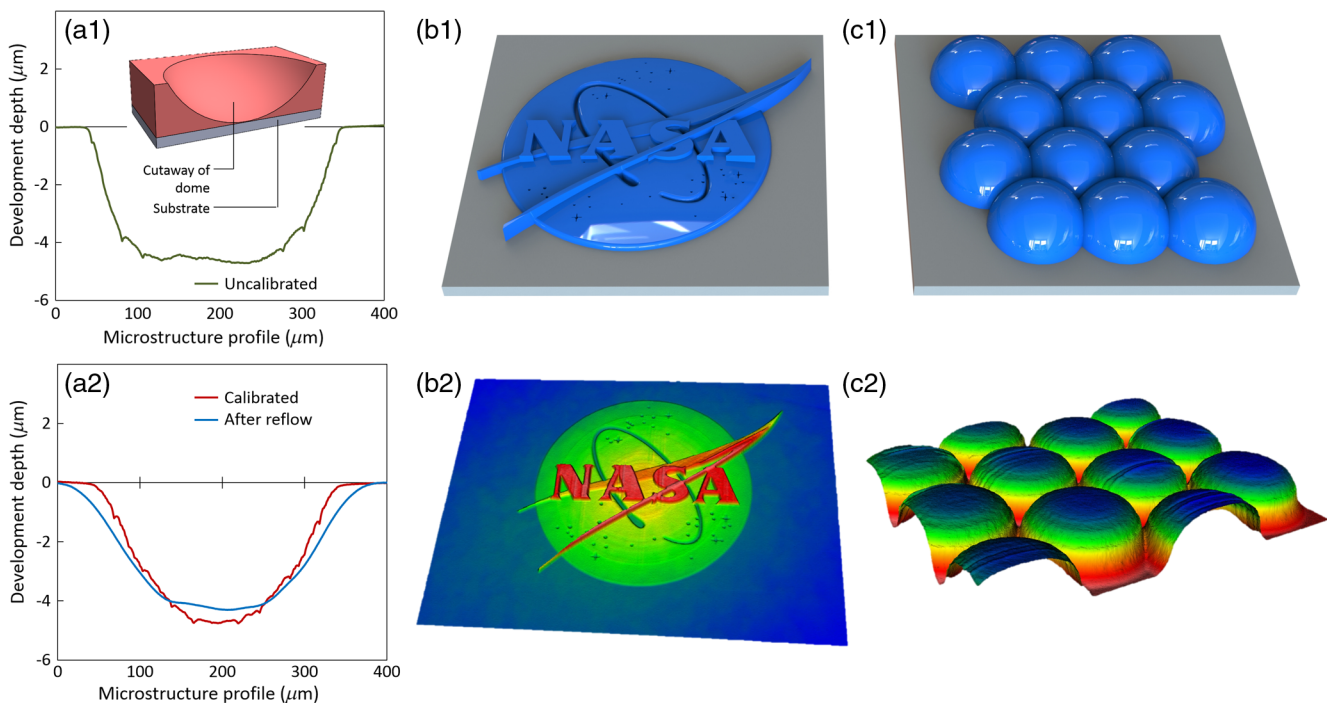


Fig. 5 Results of various grayscale fabrication samples. Profilometer scan of initial dome structure (AZ4620 photoresist) highlighting nonlinearity effects (a1) and improvements in the calibrated run (a2). CAD model of logo (b1) and interferometer scan of the fabricated microstructure (b2) $\sim 750 \mu\text{m}$ diameter $\times 3 \mu\text{m}$ height (Shipley 1827 photoresist). CAD model of hemisphere array (c1) and interferometer scan of the fabricated microstructure (c2) $\sim 800 \mu\text{m} \times 600 \mu\text{m} \times 3 \mu\text{m}$ (Shipley 1827 photoresist).

show corresponding interferometer scans of the actual fabricated structure, demonstrating some of the complex detail easily attainable using this GSC process.

The method presented here has several advantages over optical grayscale lithography, including no physical mask requirements and higher spatial resolution. The main drawback, however, the nonuniform thickness in the z resolution, affects both optical lithography using a grayscale mask and this GSC process equally. Further complicating matters is that a good predictive model of photoresist development is unavailable, requiring an added calibration step to obtain empirically-derived exposure profiles. Additionally, photoresists are considered a temporary medium and do not feature long-term mechanical stability. As such, they are generally only suitable as transfer layers or aids/masks for follow-on processing. To truly demonstrate marketplace value, the ability to transfer the complex 3-D topography to more permanent forms is required. One such ideal process is use of the photoresist as a mold like in soft lithography/microfluidics. Other transfer processes include DRIE and RIE, which can be used to create high aspect ratio structures in silicon wafers. As photoresist and silicon wafer have different DRIE etch rates, this process will allow transfer of the 3-D surface geometry from the relatively low aspect ratio temporary designs (in photoresist) into high aspect ratio permanent ones (in silicon). A third possibility is using a photosensitive polyimide film in lieu of photoresist. Other further innovations are also possible, such as incorporating multistep fabrication processes to enable undercut features, as well as development of photoresist “lift-off” process to generate freestanding structures.

4 Summary and Conclusion

In this paper, we presented development of a simple process and associated software conversion utility for creating grayscale mask files appropriate for fabricating complex 3-D surface morphologies using direct-write lithography. This conversion method and the corresponding software allows for creation of structures in commonly available and widely used CAD software, which are ideally suited for designing complex 3-D surfaces. The automated conversion from CAD file to LPG-compatible DXF file removes one of the key hindrances to grayscale lithography, time consuming mask file creation. To the best of the authors’ knowledge, no similar methods exist. Therefore, this GSC software fulfills a niche for a simplistic, easy-to-implement automated method capable of generating and fabricating complex 3-D microstructures using grayscale lithography. Additionally, a wide variety of alternate representations of mask data may be conceived. Therefore, this process is not solely limited to the particular implementation presented here. This GSC process and the demonstrated software utility will help lower the barrier to entry for grayscale lithography and fuel breakthroughs in fields such as popup (origami) MEMS, miniaturized biomedical sensors with greater sensitivity due to enhanced mixing (made available from microblades), MEMS bistable devices, and micro 3-D printing.

Acknowledgments

This research was partially funded by NSF EPSCoR Award number 0814194. The authors also wish to acknowledge the

University of Louisville MNTC and cleanroom staff for their assistance with numerous fabrication processes.

References

1. Yole Développement, *Status of the MEMS Industry 2015*, Yole Développement, Villeurbanne, France (2015).
2. E. Mounier, “MEMS markets & applications,” in *W2nd Workshop on design, control and software implementation for distributed MEMS*, Besancon, France (2012).
3. L. Hardesty, “How to corner the MEMS market,” *MIT News* (2012). <http://news.mit.edu/2012/manufacturing-mems-production-0405> (5 April 2012)
4. D. Deslandes and K. Wu, “Single-substrate integration technique of planar circuits and waveguide filters,” *IEEE Trans. Microwave Theory Tech.* **51**(2), 593–596 (2003).
5. J. Bhardwaj, H. Ashraf, and A. McQuarrie, “Dry silicon etching for MEMS,” in *Proc. Symp. Microstructures and Microfabricated Systems* Vol. 97, pp. 118–130 (1997).
6. N. Tea et al., “Hybrid postprocessing etching for CMOS-compatible MEMS,” *J. Microelectromech. Syst.* **6**(4), 363–372 (1997).
7. J. Haneveld et al., “Wet anisotropic etching for fluidic 1D nanochannels,” *J. Microelectromech. Syst.* **13**(4), S62–S66 (2003).
8. Y. Zhang et al., “Designable 3D nanofabrication by femtosecond laser direct writing,” *Nano Today* **5**(5), 435–448 (2010).
9. T. Katoh et al., “Direct writing for three-dimensional microfabrication using synchrotron radiation etching,” *Sens. Actuators A Phys.* **89**(1–2), 10–15 (2001).
10. C. Guo et al., “Grayscale photomask fabricated by laser direct writing in metallic nano-films,” *Opt. Express* **17**(22), 19981–19987 (2009).
11. K. Hon, L. Li, and I. Hutchings, “Direct writing technology—advances and developments,” *CIRP Ann.—Manuf. Technol.* **57**(2), 601–620 (2008).
12. H. Lorenz et al., “High-aspect-ratio, ultrathick, negative-tone near-UV photoresist and its applications for MEMS,” *Sens. Actuators A Phys.* **64**(1), 33–39 (1997).
13. Y. Yoon, J. Park, and M. Allen, “Multidirectional UV lithography for complex 3-D MEMS structures,” *J. Microelectromechanical Syst.* **15**(5), 1121–1130 (2006).
14. A. Ayon et al., “Tailoring etch directionality in a deep reactive ion etching tool,” *J. Vac. Sci. Technol. B* **18**(3), 1412–1416 (2000).
15. T. Chou and K. Najafi, “Fabrication of out-of-plane curved surfaces in Si by utilizing RIE lag,” in *IEEE Int. Conf. Microelectromechanical Systems*, pp. 145–148 (2002).
16. C. Waits et al., “Microfabrication of 3D silicon MEMS structures using gray-scale lithography and deep reactive ion etching,” *Sens. Actuators A Phys.* **119**(1), 245–253 (2005).
17. T. Bourouina, T. Masuzawa, and H. Fujita, “The MEMSNAS process: Microlading effect for micromachining 3-D structures of nearly all shapes,” *J. Microelectromech. Syst.* **13**(2), 190–199 (2004).
18. J. Bustillo, R. Howe, and R. Muller, “Surface micromachining for microelectromechanical systems,” *Proc. IEEE* **86**, 1552–1574 (1998).
19. C. Ahn and M. Allen, “Micromachined planar inductors on silicon wafers for MEMS applications,” *IEEE Trans. Ind. Electron.* **45**(6), 866–876 (1998).
20. M. Schmidt, “Wafer-to-wafer bonding for microstructure formation,” *Proc. IEEE* **86**, 1575–1585 (1998).
21. D. Sparks et al., “Wafer-to-wafer bonding of nonplanarized MEMS surfaces using solder,” *J. Microelectromech. Syst.* **11**(6), 630–634 (2001).
22. S. Azimi et al., “Formation of three-dimensional and nanowall structures on silicon using a hydrogen-assisted high aspect ratio etching,” *J. Vac. Sci. Technol. B Microelectron. Nanometer Struct.* **28**(6), 1125–1131 (2010).
23. M. Lecompte, X. Gao, and D. Prather, “Photoresist characterization and linearization procedure for the gray-scale fabrication of diffractive optical elements,” *Appl. Opt.* **40**(32), 5921–5927 (2001).
24. R. Kirchner et al., “Bio-inspired 3D funnel structures made by grayscale electron-beam patterning and selective topography equilibration,” *Microelectron. Eng.* **141**, 107–111 (2015).
25. S. Lee and K. Anbumony, “Accurate control of remaining resist depth for nanoscale three-dimensional structures in electron-beam grayscale lithography,” *J. Vac. Sci. Technol. B* **25**(6), 2008–2012 (2007).
26. H. Mekaru, “Performance of SU-8 membrane suitable for deep x-ray grayscale lithography,” *Micromachines* **6**, 252–265 (2015).
27. M. Rao, M. Aimi, and N. MacDonald, “Single-mask, three-dimensional microfabrication of high-aspect-ratio structures in bulk silicon using reactive ion etching lag and sacrificial oxidation,” *Appl. Phys. Lett.* **85**(25), 6281–6283 (2004).
28. D. O’Shea and W. Rockward, “Gray-scale masks for diffractive-optics fabrication: II. Spatially filtered halftone screens,” *Appl. Opt.* **34**(32), 7518–7526 (1995).
29. C. Waits, A. Modafe, and R. Ghodssi, “Investigation of gray-scale technology for large area 3D silicon MEMS structures,” *J. Microelectromech. Syst.* **13**(2), 170–177 (2002).

30. J. Lake et al., “Maskless grayscale lithography using a positive-tone photodefinable polyimide for MEMS applications,” *J. Microelectromech. Syst.* **20**(6), 1483–1488 (2011).
31. V. Nock and R. Blaikie, “Fabrication of optical grayscale masks for tapered microfluidic devices,” *Microelectron. Eng.* **85**(5–6), 1077–1082 (2008).
32. A. Waldbaur et al., “Maskless projection lithography for the fast and flexible generation of grayscale protein patterns,” *Small* **8**(10), 1570–1578 (2012).
33. Y. Yamanishi et al., “Fabrication and application of 3-D magnetically driven microtools,” *J. Microelectromech. Syst.* **19**(2), 350–356 (2010).
34. R. Kirchner and H. Schiff, “The ascent of high resolution and high volume 3D replication,” *Microelectron. Eng.* **141**, 243–244 (2015).
35. 3D Systems, Inc., “Stereolithography interface specification,” Valencia, California (1988).
36. M. Szilvsi-Nagy and G. Mátyási, “Analysis of STL files,” *Math. Comput. Model.* **38**(7–9), 945–960 (2003).
37. A. Kewitsch and A. Yariv, “Nonlinear optical properties of photoresists for projection lithography,” *Appl. Phys. Lett.* **68**(4), 455–457 (1996).
38. Autodesk, Inc., *DXF Reference*, pp. 1–253, Autodesk, Inc., San Rafael, California (2011).
39. Heidelberg Instruments, *DWL 66FS User Guide Part I*, pp. 1–80, Heidelberg Instruments, Heidelberg, Germany (2007).
40. A. Emadi et al., “Vertically tapered layers for optical applications fabricated using resist reflow,” *J. Micromech. Microeng.* **19**(7), 074014 (2009).
41. S. Cho, J. Kim, and K. Oh, “Enhanced optical coupling performance in an InGaAs photodiode integrated with wet-etched microlens,” *IEEE Photonics Technol. Lett.* **14**(3), 378–380 (2002).
42. E. Park, M. Kim, and Y. Kwon, “Microlens for efficient coupling between LED and optical fiber,” *IEEE Photonics Technol. Lett.* **11**(4), 439–441 (1999).

James Loomis received his PhD in mechanical engineering from the University of Louisville in 2013. His research focused on

photomechanical actuation in nanocarbon/elastomer composites. He then joined the NanoEngineering Group at MIT as a postdoc under Professor Gang Chen. He worked there on fabrication techniques for large-area polymer films with tunable thermal conductivity and design of high efficiency concentrating solar power receivers. In 2015, he joined the faculty at the University of Auckland, New Zealand.

Dilan Ratnayake received his BSc in physics from the University of Peradeniya, Sri Lanka, in 2009 and his MSc in physics from the University of Louisville in 2012. He is currently pursuing his PhD degree in electrical and computer engineering and working as an instructor and teaching assistant. His research focuses on developing a no-power bistable MEMS temperature sensor.

Curtis McKenna received his MSc in electrical engineering in 2009 from the University of Louisville. He is currently working at the Micro/Nano Technology Center at the University of Louisville, where he maintains tools, as well as trains and assists students. His research focuses primarily on grayscale lithography.

Kevin M. Walsh received his PhD in electrical engineering (micro-electronics) from the University of Cincinnati in 1992. He is currently the Fife endowed professor of electrical and computer engineering at the University of Louisville, where he also serves as the MNTC founding director. He is cofounder of 3 startups, holds 7 patents, has taught more than 20 different courses, advised more than 25 theses, and published more than 100 papers in the areas of micro-/nanotechnology, MEMS, microfabrication, packaging, sensors, actuators, clean-room design/operation, and course development.